ELECTRONIC SUPPLEMENTARY INFORMATION (ESI) FILE

Selective placement of modifiers on hematite thin films for solar water splitting

*Fabio A. Pires [a,b]; Gabriel T. dos Santos [a,c]; Jefferson Bettini [a]; Carlos A. R. Costa [a]; Renato V. Gonçalves [d]; Ricardo H. R. Castro [e]; Flavio L. Souza [a,b,f]**

[a] Brazilian Nanotechnology National Laboratory (LNNano), Brazilian Center for Research in Energy and Materials (CNPEM) – Campinas, SP, Brazil; [b] Institute of Chemistry, State University of Campinas (UNICAMP) – Campinas, SP, Brazil; [c] Engineering School, Federal University of Rio Grande do Sul (UFRGS), RS, Brazil; [d] São Carlos Institute of Physics, University of São Paulo (USP) - São Carlos, SP, Brazil; [e] Lehigh University, Department of Materials Science and Engineering, Bethlehem, Pennsylvania, 18015; [f] Center for Natural and Human Sciences, Federal University of ABC (UFABC) – Santo André, SP, Brazil.

1 Experimental section

Figure S1 below shows how the hematite-based photoelectrodes were produced from the spin-coating polymeric precursor solution (PPS) followed by thermal treatments. See detailed information in the "Experimental section" of the main text.

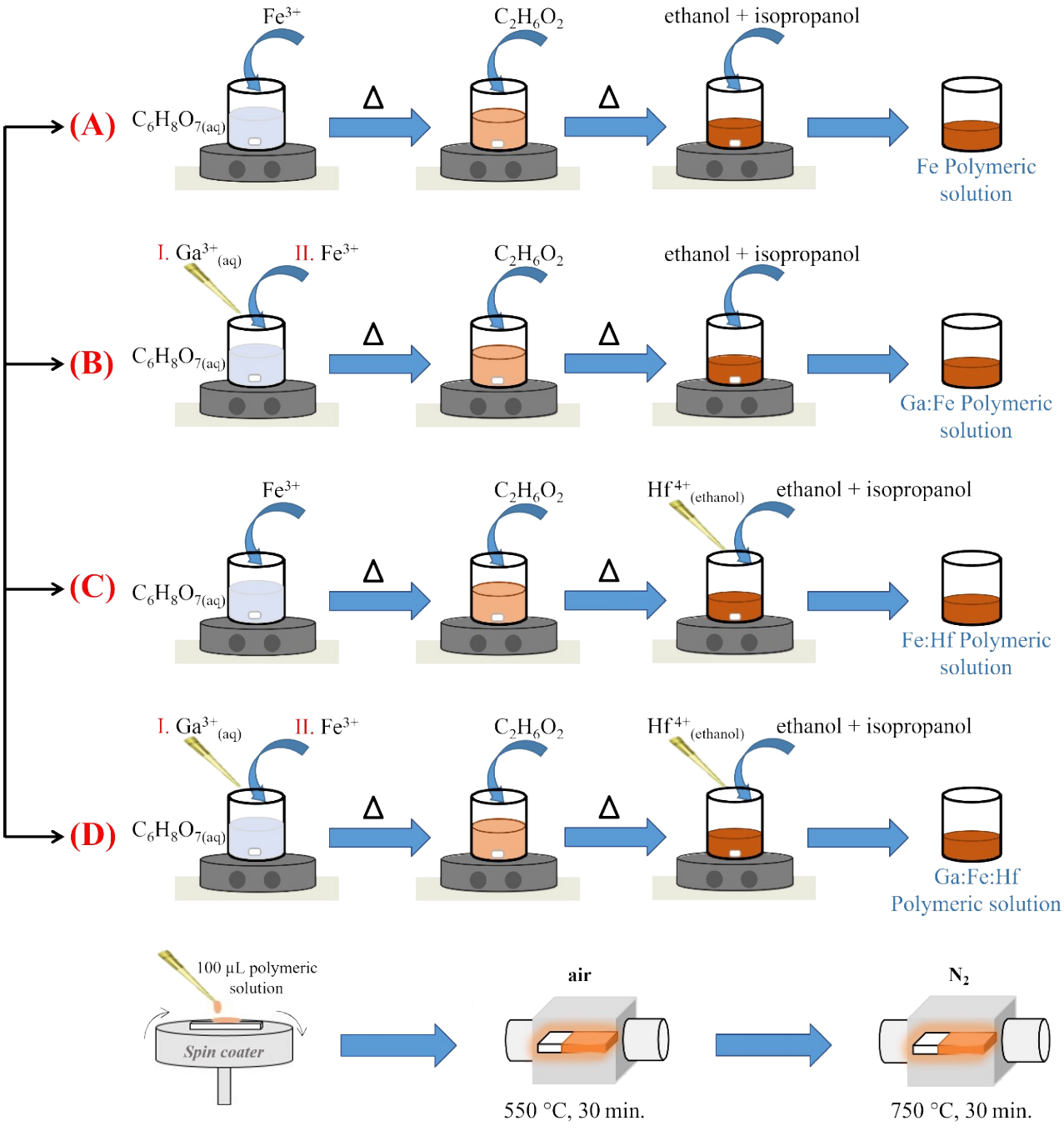

Figure S1. Schematic representation for the synthesis of (A) pristine hematite polymeric precursor, (B) Ga:Fe_2O_3 precursor, (C) Fe_2O_3:Hf precursor and (D) Ga:Fe_2O_3:Hf precursor. The precursor solutions were spin-coated onto FTO substrate surface and underwent two thermal treatments.

2 Structural characterization

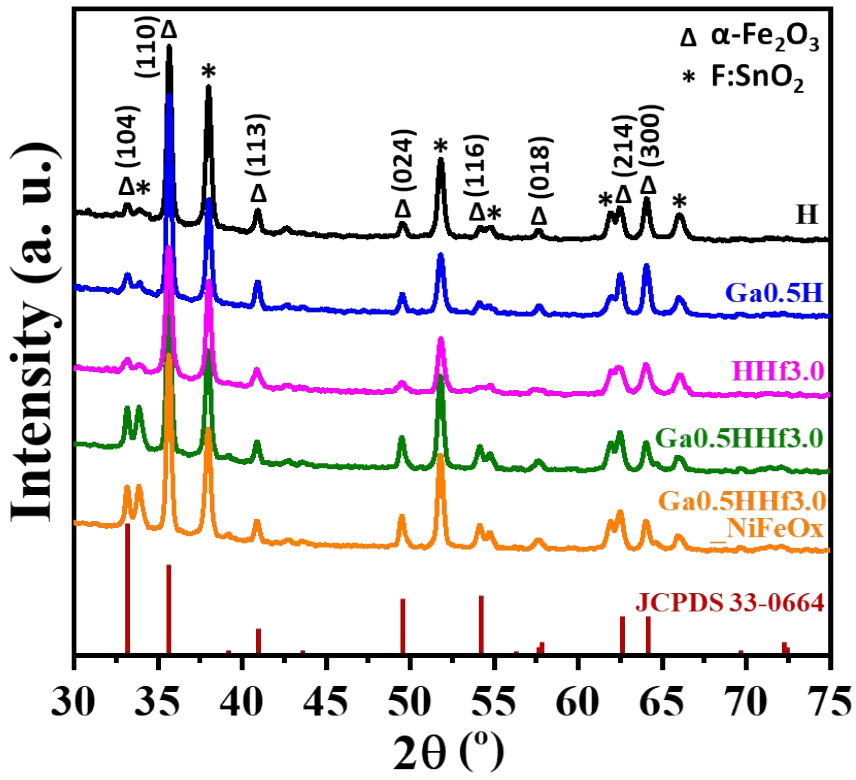

Figure S2. X-ray diffraction pattern of pristine hematite, GaH photoanodes, HHf3.0, Ga0.5HHf3.0 and Ga0.5HHf3.0_$NiFeO_x$ photoanodes.

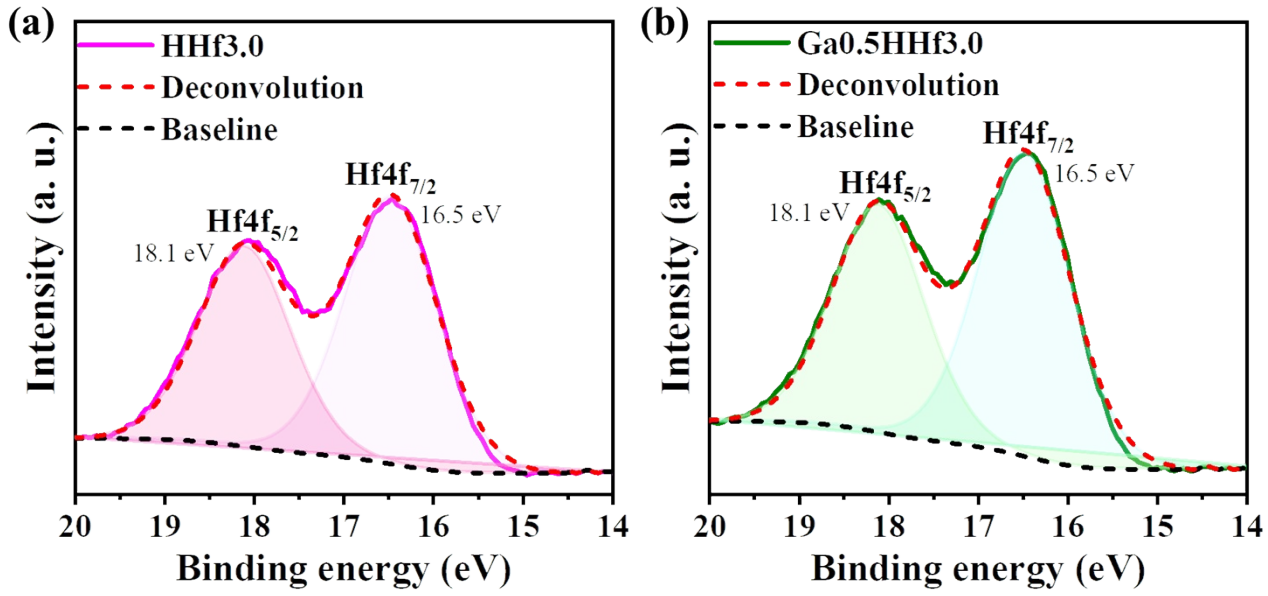

Figure S3. Deconvolutions of Hf 4f high-resolution XPS spectra of **(a)** HHf3.0 and **(b)** Ga0.5HHf3.0 photoanodes.

3 Optical characterization

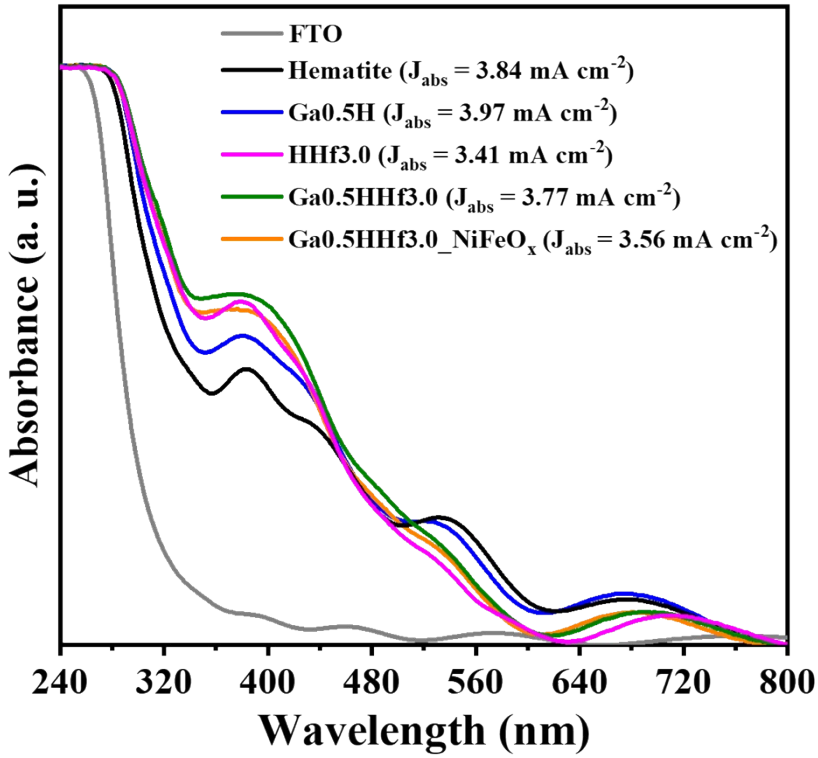

Figure S4. Absorbance spectra and J_{abs} calculated values of pristine hematite, GaH photoanodes, HHf3.0, Ga0.5HHf3.0 and Ga0.5HHf3.0_$NiFeO_x$ photoanodes.

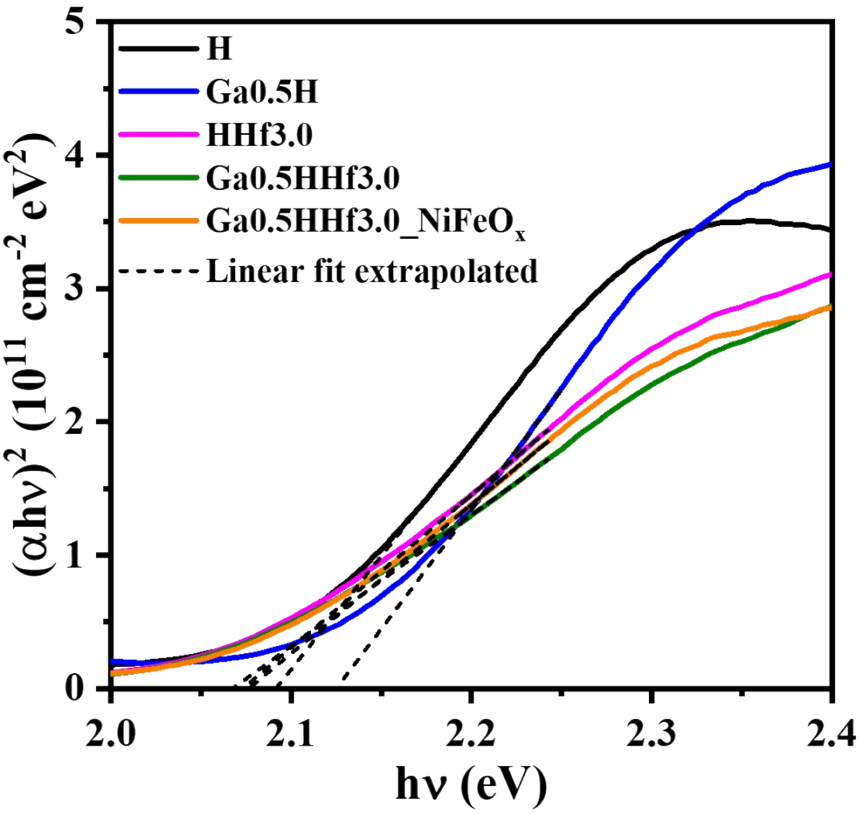

Figure S5. Tauc plots of pristine hematite, GaH photoanodes, HHf3.0, Ga0.5HHf3.0 and Ga0.5HHf3.0_$NiFeO_x$ photoanodes, calculated from equation 2 shown in the main text.

Table S1. Optical band gap values estimated from Tauc plots.

Sample	E_g (eV)
H	2.09
Ga0.5H	2.13
HHf3.0	2.07
Ga0.5HHf3.0	2.07
Ga0.5HHf3.0_$NiFeO_x$	2.08

4 Photoelectrochemical optimization

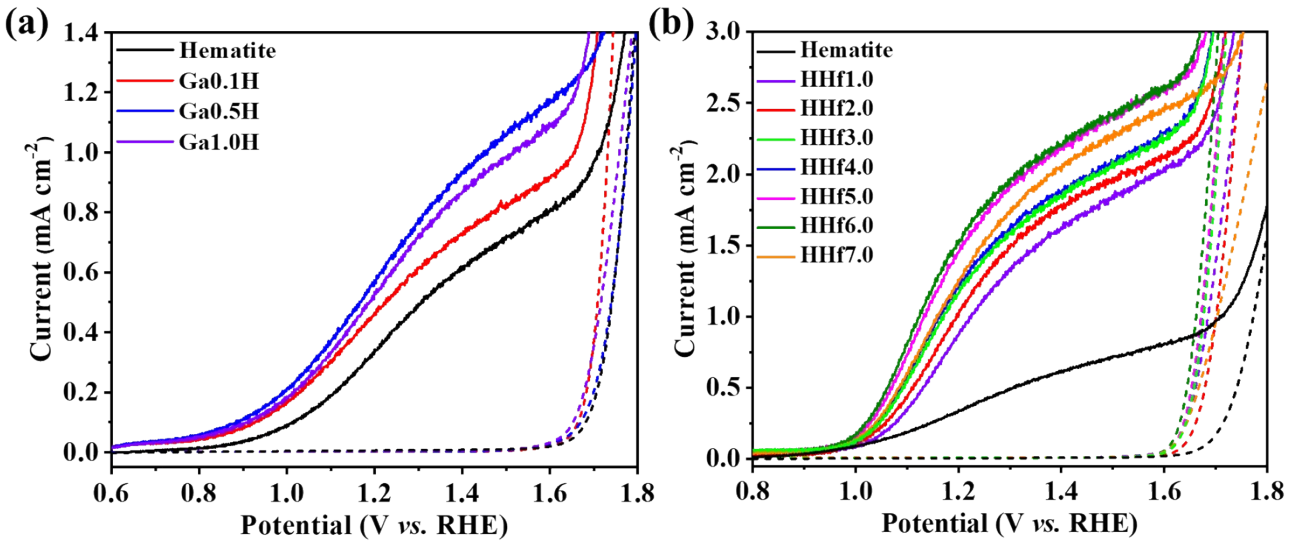

Figure S6. (a) Photocurrent curves of pristine hematite and Ga-modified photoanodes. **(b)** Photocurrent values of pristine hematite and Hf-modified photoanodes. The concentrations chosen for case study were 0.5% Ga^{3+} (best performance among gallium single-modified photoanodes) and 3.0% Hf^{4+} (to avoid the possibility of second phase formation).

5 Literature review

Table S2 presents some state-of-art highest performances reported for hematite-based photoanodes. The predominance of solvothermal/hydrothermal methods remarks the morphology-dependent paradigm. Multi-step protocols and elevated thickness are needed for enhanced performance. Our work introduces a single deposition of the polymeric precursor solution followed by catalyst incorporation, producing an ultra-thin photoanode with near benchmark light-to-current conversion. The data was extracted from the Scopus Database® repository.

Table S2. Selected state-of-art works reporting the highest photoelectrochemical performances for hematite-based photoanodes in comparison to the optimized photoanode from this work.

Photoanode	Method	Thickness (nm)	Photocurrent at 1.23 V_{RHE} (mA cm^{-2})	Conditions	Ref.
Ga0.5HHf3.0_NiFeO$_x$ (this work)	**spin-coating polymeric precursor**	**176 ±29**	**2.30**	**NaOH 1M, 100 mW cm^{-2}**	-
Fe_2O_3-H_2/TiO_2-H_2/CoP_i	hydrothermal	≈ 730	6.00	KOH 1M, 100 mW cm^{-2}	[4]
P-Hf-Fe_2O_3/FeNiOOH	hydrothermal, immersion bath, electrodeposition	≈ 250	5.24	NaOH 1M, 100 mW cm^{-2}	[5]
Fe_2O_3-SnO_x	hydrothermal and ALD (20 cycles)	≈ 354	3.12	NaOH 1M, 100 mW cm^{-2}	[65]
E–Ti–Fe_2O_3/CoP_i	hydrothermal, electrodeposition and KOH treatment	not informed	4.10	NaOH 1M, 100 mW cm^{-2}	[66]
WN-α-Fe_2O_3/Co_3O_4	hydrothermal	≈ 540	3.48	KOH 1M, 100 mW cm^{-2}	[67]
Fe_2O_3/TiO_2/C/β-FeOOH	hydrothermal	≈ 600	2.95	KOH 1M, 100 mW cm^{-2}	[68]
n-Ce-Fe_2O_3/p-Cu_2O/ FeOOH	hydrothermal	≈ 630	4.20	KOH 1M, 100 mW cm^{-2}	[69]
CoP_i/Ca-Fe_2O_3/Fe_2O_3/Pt	hydrothermal	≈ 635	2.94	NaOH 1M, 100 mW cm^{-2}	[70]
FeGe1	hydrothermal	~1000	3.20	NaOH 1M, 100 mW cm^{-2}	[71]
Ti–Fe_2O_3 MC/CoP_i	Solvothermal self-assembling and spin coating	1500	3.50	NaOH 1M, 100 mW cm^{-2}	[72]
MC_T/Fe_2O_3(Ti)/CoP_i	Solvothermal and spin coating	1600	5.50	NaOH 1M, 100 mW cm^{-2}	[73]

Table S3 summarizes the main recent (2019-2023) results found for co-doped (dual modified) hematite-based photoanodes in the Scopus Database® repository. Once again, state-of-art works only

employ hydrothermal routes in the production of the photoanodes. The search entries used were: hematite co-doping; hematite dual modification; hematite dual modified.

Table S3: Main recent (2019-2023) results found for co-doped (dual modified) hematite-based photoanodes in the Scopus Database® repository in comparison to the optimized photoanode from this work.

Photoanode	Method	Thickness (nm)	Photocurrent at 1.23 V_{RHE} (mA cm^{-2})	Conditions	Ref.
Ga0.5HHf3.0_$NiFeO_x$ (this work)	**spin-coating polymeric precursor**	**176 ±29**	**2.30**	**NaOH 1M, 100 mW cm^{-2}**	-
P-Ti-Fe_2O_3	hydrothermal	~450	2.56	NaOH 1M, 100 mW cm^{-2}	[15]
(Ti,Zr)-Fe_2O_3	hydrothermal	~700	1.51	NaOH 1M, 100 mW cm^{-2}	[22]
Ti,Zn-Fe_2O_3	hydrothermal	not informed	1.02	NaOH 1M, 100 mW cm^{-2}	[24]
Al(Zr-Fe_2O_3)/CoP_i	hydrothermal	~370	1.80	NaOH 1M, 100 mW cm^{-2}	[25]
Nb-Zr:Fe_2O_3	hydrothermal	~280	2.05	NaOH 1M, 100 mW cm^{-2}	[27]
N-Sn-Fe_2O_3/CoP_i	hydrothermal	not informed	2.87	NaOH 1M, 100 mW cm^{-2}	[28]
F,Ti:Fe_2O_3	hydrothermal	~515	1.61	NaOH 1M, 100 mW cm^{-2}	[29]
F,Zr:Fe_2O_3	hydrothermal	~273	1.91	NaOH 1M, 100 mW cm^{-2}	[30]
Zr,Al-Fe_2O_3/CoO_x	hydrothermal	339-397	1.50	NaOH 1M, 100 mW cm^{-2}	[74]
Ti_i-Pt_e-M-NiFe	hydrothermal, methanol treatment	400-450	2.81	NaOH 1M, 100 mW cm^{-2}	[75]
Pt/Al-HT	microwave hydrothermal	~544	1.55	NaOH 1M, 100 mW cm^{-2}	[76]

6 Reproducibility analysis

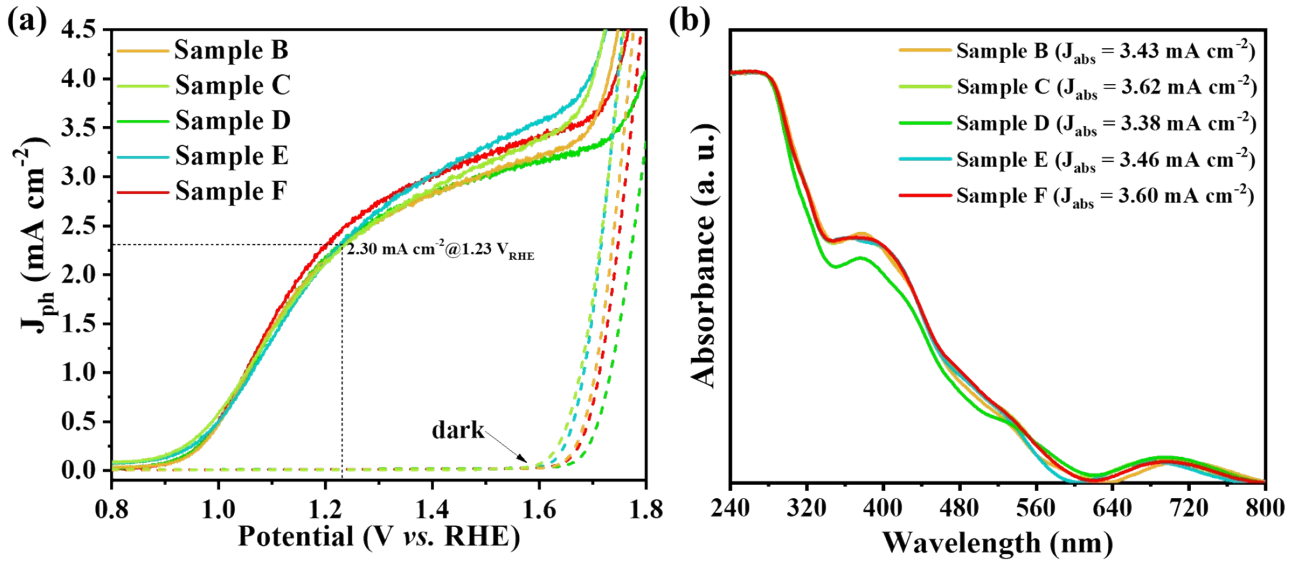

Figure S7. Reproducibility analysis of Ga0.5HHf3.0_NiFeO$_x$ photoanode. Samples named as B and C were produced from the same polymeric solution of the extensively characterized sample presented in the main text (called "A") and samples D, E and F were produced from a polymeric solution later synthesized with the purpose to evaluate its reproducibility. **(a)** LSV measurements show the polymeric precursor solution (PPS) method can deliver materials with reproducible performance. **(b)** Absorbance measurements show the method capability to deliver materials with reproducible optical properties.

7 Stability of the optimized photoanode

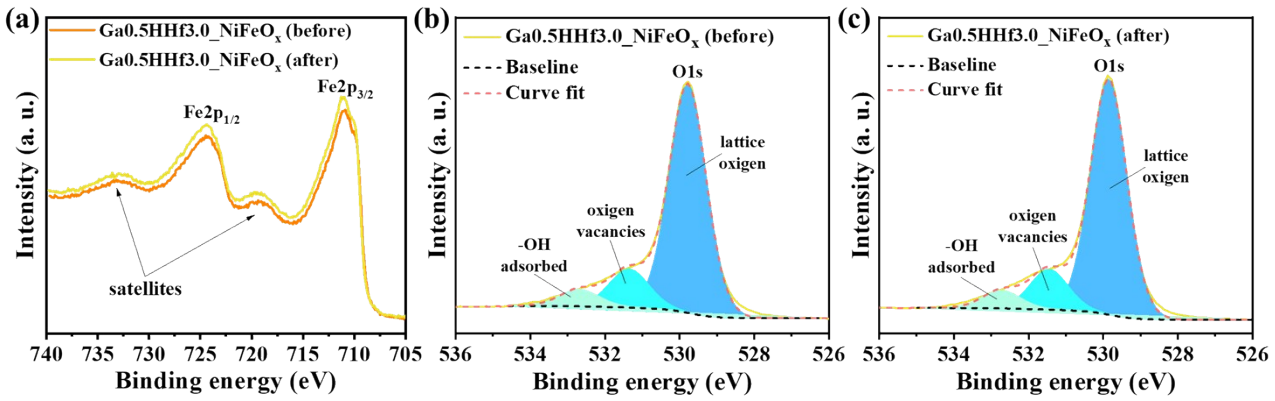

Figure S8. a) Iron high-resolution XPS spectra of Ga0.5HHf3.0_NiFeO$_x$ photoanode before and after PEC operation for 3h under illumination. **b)** Deconvoluted oxygen high-resolution XPS spectra of Ga0.5HHf3.0_NiFeO$_x$ photoanode before stability test. **c)** Deconvoluted oxygen high-resolution XPS spectra of Ga0.5HHf3.0_NiFeO$_x$ photoanode after stability test.

Table S4. Percentages of lattice oxygen, oxygen vacancies and -OH adsorbed in the surface of Ga0.5HHf3.0_$NiFeO_x$ photoanode before and after PEC operation for 3h under illumination.

Specie assigned	Binding energy (eV)	Ga0.5HHf3.0_$NiFeO_x$ before (%)	Ga0.5HHf3.0_$NiFeO_x$ after (%)
Metal-O	529.8	79.46	79.41
$V_O^{\cdot\cdot}$	531.4	14.30	14.22
-OH adsorbed	532.7	6.24	6.37

8 Charge carrier dynamics analysis

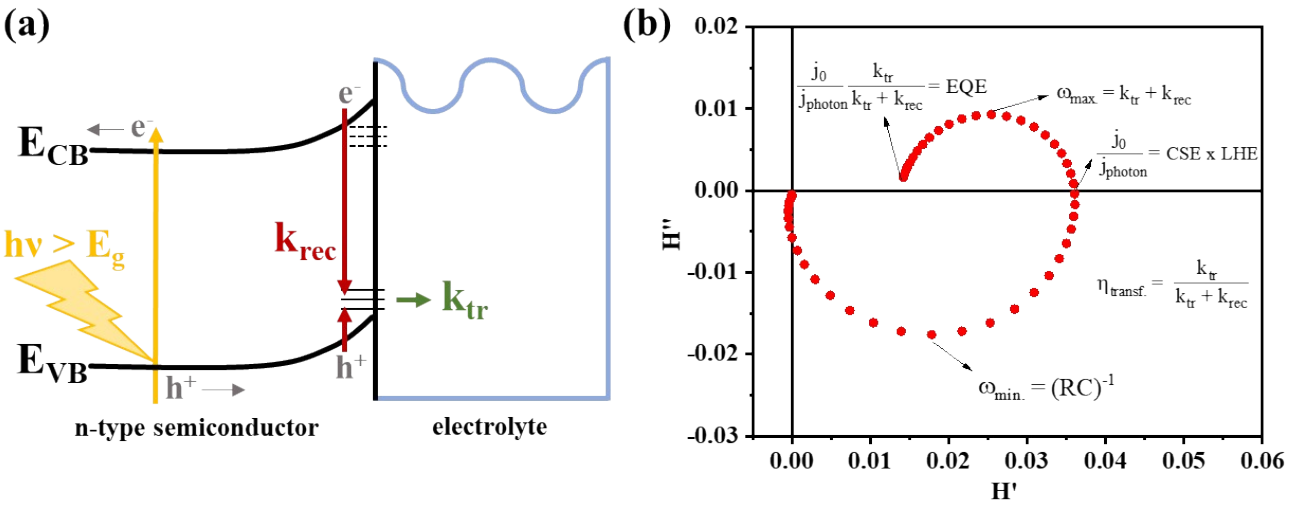

Figure S9. a) Band diagram representing the photoelectrochemical processes considered in the IMPS general theory calculations in the presence of surface states. Photogenerated holes can be trapped at the surface and subsequently either recombine with electrons (k_{rec}) or be transferred to the electrolyte (k_{tr}). Majority carriers (e^-) may also be trapped at the surface (k_{rec}). **b)** IMPS Nyquist plot and calculations of IMPS parameters and efficiencies following the general theory [79], where j_0 is the amplitude of the modulated photocurrent (electrons cm^{-2} s^{-1}), j_{photon} is the incident photon flux (photons cm^{-2} s^{-1}), k_{tr} is the charge transfer rate constant, k_{rec} is the surface recombination rate constant, $(RC)^{-1}$ is the cell time constant, and $\omega_{min.}$ and $\omega_{max.}$ are the frequencies for minimum and maximum H'' values of IMPS Nyquist plots.

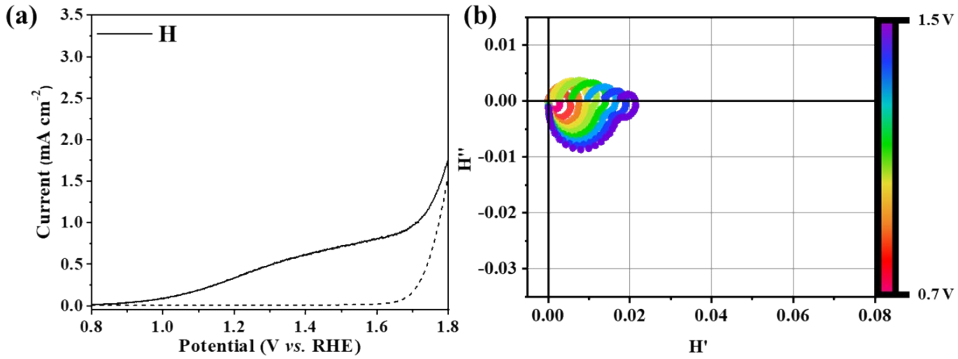

Figure S10. a) Pristine hematite photocurrent density profile. **b)** Intensity modulated photocurrent spectroscopy (IMPS) plots of pristine hematite measured from 0.7 V to 1.5V, with a step of 0.1 V.

9 Electronic structure analysis – UPS

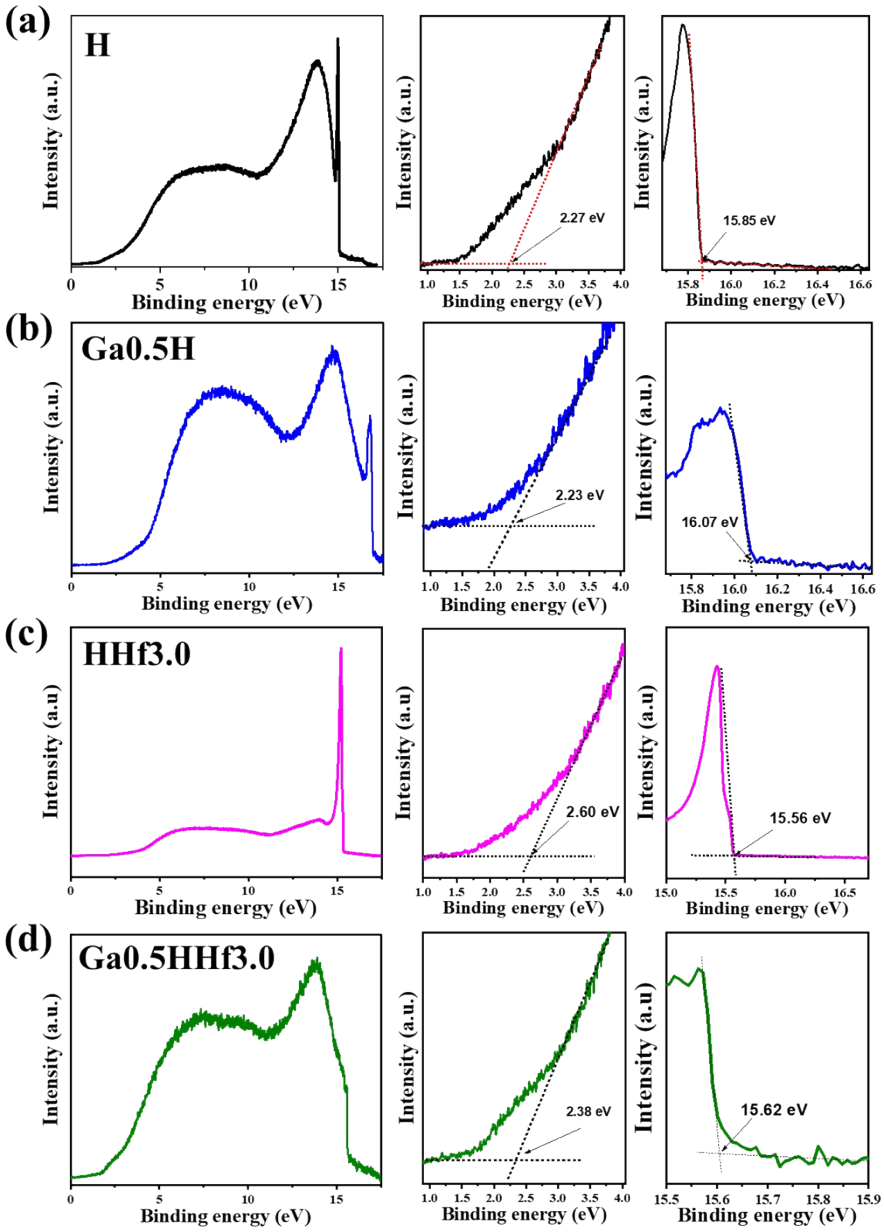

Figure S11. He I UPS data for **a)** H, **b)** Ga0.5H, **c)** HHf3.0, and **d)** Ga0.5HHf3.0 photoanodes at 298 K. The plots to the right of each UPS spectrum represent the expansion of the region near the Fermi level and the determination of the secondary electron cutoff, respectively. The sample bias was – 4.00 V relative to ground.